ADVANCED MATERIALS
www.advmat.de

Check for updates

Ionic Liquid Gating Control of Spin Reorientation Transition and Switching of Perpendicular Magnetic Anisotropy

Shishun Zhao, Lei Wang, Ziyao Zhou, Chunlei Li, Guohua Dong, Le Zhang, Bin Peng, Tai Min, Zhongqiang Hu, Jing Ma, Wei Ren, Zuo-Guang Ye, Wei Chen, Pu Yu, Ce-Wen Nan, and Ming Liu**

Electric field (E-field) modulation of perpendicular magnetic anisotropy (PMA) switching, in an energy-efficient manner, is of great potential to realize magnetoelectric (ME) memories and other ME devices. Voltage control of the spin-reorientation transition (SRT) that allows the magnetic moment rotating between the out-of-plane and the in-plane direction is thereby crucial. In this work, a remarkable magnetic anisotropy field change up to 1572 Oe is achieved under a small operation voltage of 4 V through ionic liquid (IL) gating control of SRT in Au/[DEME]$^+$[TFSI]$^-$/Pt/(Co/Pt)$_2$/Ta capacitor heterostructures at room temperature, corresponding to a large ME coefficient of 378 Oe V^{-1}. As revealed by both ferromagnetic resonance measurements and magnetic domain evolution observation, the magnetization can be switched stably and reversibly between the out-of-plane and in-plane directions via IL gating. The key mechanism, revealed by the first-principles calculation, is that the IL gating process influences the interfacial spin–orbital coupling as well as net Rashba magnetic field between the Co and Pt layers, resulting in the modulation of the SRT and in-plane/out-of-plane magnetization switching. This work demonstrates a unique IL-gated PMA with large ME tunability and paves a way toward IL gating spintronic/electronic devices such as voltage tunable PMA memories.

Tailoring the interfacial magnetism as well as perpendicular magnetic anisotropy (PMA) switching in a fast, reversible, and energy-efficient manner is one of the fundamental importance in realizing voltage controllable spintronics/electronics devices,[1–7] for example, next generation of magnetoelectric (ME) PMA memories with enhanced thermal stability and ultrahigh storage density.[8,9] The key step to realize this goal is to modulate spin-reorientation transition (SRT) electrically, allowing voltage-induced magnetization switches between the in-plane and out-of-plane directions. For decades, most of the voltage-control magnetization switching were driven by the strain-mediated ME coupling effect.[10,11] However, the strain effect-induced magnetic easy axis rotation (magnetization switching) in the magnetic film plane or the voltage control of SRT process were usually limited by the strong demagnetization field arising from shape anisotropy as well as the relative weak ME tunability.[10–13]

Recently, the ionic liquid (IL) gating process has been rapidly developed for E-field-driven material properties modification, as shown by the schematic representation in **Figure 1**a, by using a capacitor structure.[6,14–23] The ionic liquid (IL) gating process manipulates magnetic properties as demand, like magnetic resistance[7,21] and spin transfer torque,[24] due to

S. Zhao, Prof. Z. Zhou, C. Li, G. Dong, L. Zhang, Dr. B. Peng, Prof. Z. Hu, Prof. W. Ren, Prof. Z.-G. Ye, Prof. M. Liu
Electronic Materials Research Laboratory
Key Laboratory of the Ministry of Education and International Center for Dielectric Research
School of Electronic and Information Engineering
Xi'an Jiaotong University
Xi'an 710049, China
E-mail: ziyaozhou@xjtu.edu.cn; mingliu@xjtu.edu.cn

Dr. L. Wang, Prof. T. Min
Center for Spintronics and Quantum System
State Key Laboratory for Mechanical Behavior of Materials
School of Materials Science and Engineering
Xi'an Jiaotong University
Xi'an 710049, China

Prof. J. Ma, Prof. C.-W. Nan
State Key Laboratory of New Ceramics and Fine Processing and School of Materials Science and Engineering
Tsinghua University
Beijing 100084, China

Prof. Z.-G. Ye
Department of Chemistry and 4D LABS
Simon Fraser University
Burnaby, British Columbia V5A 1S5, Canada

Dr. W. Chen
Materials Science Division
Argonne National Laboratory
9700 Cass Avenue, Lemont, IL 60439, USA

Dr. W. Chen
Institute for Molecular Engineering
The University of Chicago
5640 South Ellis Avenue, Chicago, IL 60637, USA

Prof. P. Yu
State Key Laboratory of Low Dimensional Quantum Physics and Department of Physics
Tsinghua University
Beijing 100084, China

DOI: 10.1002/adma.201801639

© 2018 WILEY-VCH Verlag GmbH & Co. KGaA, Weinheim

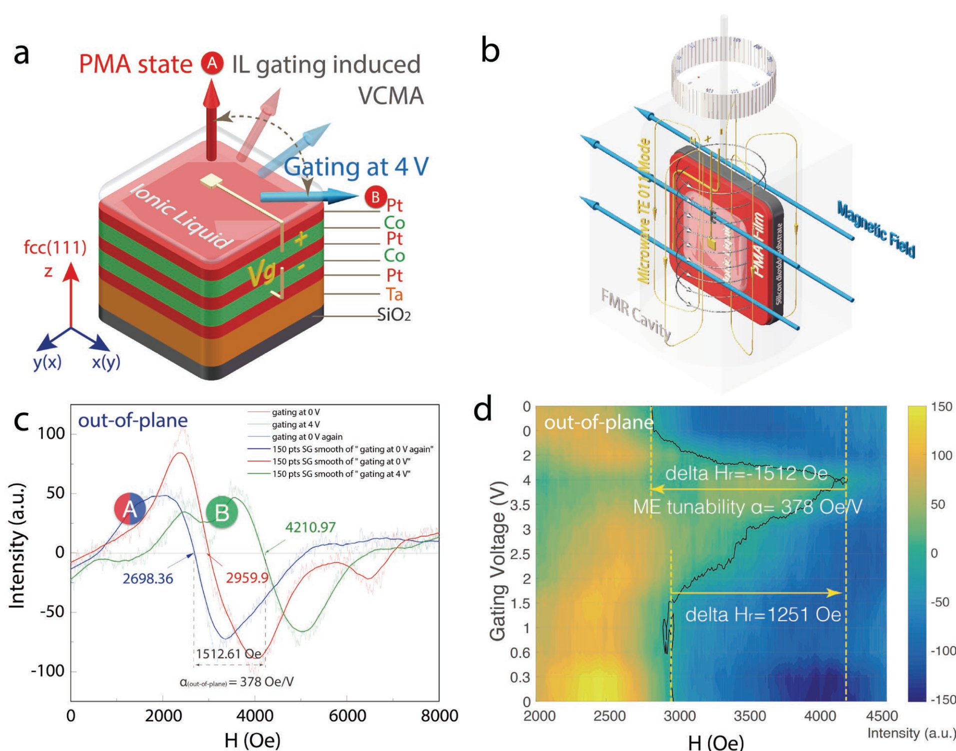

Figure 1. The in situ IL gating control PMA switching EPR measurement. a) The schematic representation of the ionic liquid gating-induced magnetization switching between PMA state A and gating state B in a typical capacitor structure. The arrows illustrate the magnetic moments rotation during the gating process. b) The schematic representation of the in situ ESR measurement. The blue arrows illustrate the external magnetic field. The closed yellow curves and black curves mark the distribution of the magnetic field component and the electric field component of the TE_{011} mode microwave, respectively. With the assistance of the rotator, the voltage control magnetic anisotropy is observed in situ at room temperature in nitrogen gas protection. The in-plane direction, in which the magnetic field is parallel to the film plane, is defined as 0°. 90° marks the out-of-plane direction. c) The out-of-plane FMR spectrums observed at initial 0 V (thin-red line), 4 V (thin-green line), and final 0 V (thin-blue line), respectively. The thicker lines demonstrate the Savitzky–Golay smoothing results of the data from thin-light lines, correspondingly. The arrows point to the resonance fields. d) The FMR phase diagram in the PMA gating process. The FMR intensity is plotted as a function of the external magnetic field (H) and the gating voltage (V_g) and scaled by the contour map. The dark black line marks the resonance field (H_r) shifts during the voltage sweeping.

electric double layer (EDL)-induced large interfacial charge doping or controllable electrochemical reaction.[25,26] For example, Yu and co-workers realized triphase transition by modulating the insertion and extraction of oxygen and hydrogen ions independently in oxide thin films via IL gating.[26] One crucial advantage of IL gating control lies in the much smaller operating voltage (V_g) (<5 V),[6,14–23] compared with conventional strain effect in bulk multiferroics that requires a large V_g up to 400–600 V.[10–13] Additionally, the IL gating control process operates at room temperature (RT) without providing extra thermal energy to overcome the oxidation energy barrier.[27,28]

In magnetic thin-film heterostructures, the interfacial electrostatic doping may effectively influence the orbital potential near the Fermi level and result in a magnetic anisotropy change via spin–orbital coupling (SOC).[29] Therefore, IL gating of Co/Pt PMA heterostructure that contains interfacial SOC is expected. In this case, a Co/Pt PMA heterostructure near the SRT state was prepared for easier magnetization rotation.[30] At this SRT state, the IL/PMA film interfacial charges from IL gating can tip the transition balance and the SOC, leading to a giant ME coupling effect and in-plane/out-of-plane magnetization switching. Nevertheless, few in situ analysis of IL gating SRT has been demonstrated,[19] because it is often difficult to determine the voltage control of magnetic anisotropy (VCMA) change quantitatively and visually due to the weak signal of ultrathin magnetic films and complex IL chemical composition.

In this work, a typical capacitor heterostructure of Au/IL/Pt/$(Co/Pt)_2$/Ta/Si was prepared with *N*,*N*-diethyl-*N*-methyl(2-methoxyethyl) ammonium bis(trifluoromethylsulfonyl)-imide ($[DEME]^+[TFSI]^-$, $[]^+$ added for the electrical property) as the gating dielectric layer and the Co/Pt PMA film as the bottom electrode. Under a small gating voltage (V_g) of 4 V, a giant VCMA of 1572 Oe was obtained by quantitative electron spin resonance (ESR) analysis, corresponding to a much larger ME coefficient (378 Oe V^{-1}) than those observed in strain-mediated ME coupling systems, such as Fe_3O_4/PZNPT (≈2.16 Oe V^{-1}),[31] FeGaB/PZNPT (≈4 Oe V^{-1})[11,12] Terfenol-D/PZNPT (≈11.6 Oe V^{-1}),[32] and other IL gating systems like Au/$[DEME]^+[TFSI]^-$/Co system (≈146 Oe V^{-1}).[25] More importantly, with a 4 V gating voltage, the magnetic easy axis can be completely switched from the out-of-plane direction to the in-plane direction in a reversible manner, indicating a remarkable voltage control of the SRT. It is worthy to mention that

 © 2018 WILEY-VCH Verlag GmbH & Co. KGaA, Weinheim

this ME coefficient (Oe V^{-1}) definition is more useful than traditional ME coefficient (Oe cm kV^{-1}) in real applications, where applied voltage is essential instead of E-field strength. Here, the ESR method serves as a precise technique that determines the VCMA within 1 Oe accuracy. The spatial magnetic anisotropy as well as VCMA change during the gating process was systemically analyzed by this ESR method correspondingly. We then developed the in situ magneto-optical Kerr effect microscopy (MOKE) as well as in situ VSM observation of the IL gating process, which accurately characterized the magnetization switched between out-of-plane and in-plane orientations in a reversible manner and revealed the E-field-induced magnetic domain evolution accordingly. In addition, the first-principles calculation was performed to reveal the physics picture of voltage control of SRT. Such large ME tunability comes from the modulation of the spin–orbital coupling energy through the Pt and Co layers, and the accompanying asymmetrical interfacial Rashba magnetic field induced by E-field will introduce a nonzero in-plane magnetization, which drives the total perpendicular magnetization toward in-plane direction. Comparing with the previous gating control Co magnetic anisotropy work, an up to 1572 Oe ME tunability has been achieved by the virtue of gating control 90° easy axis rotation, which is seven times greater than the number from our previous Co gating work. This IL gating control process was confirmed not only by in situ electron paramagnetic resonance (EPR) spectrometry quantitatively like what has been utilized in the Co work, but also with in situ VSM and MOKE measurement. Furthermore, the mechanism is also very different from that observed in our previous work, in which only the Fermi level of Co was modulated.[25] The IL gating process, a truly powerful method allowing remarkable SRT switching by a low V_g, provides a tremendous potential in magnetoelectric random access memories and other related voltage-tunable spintronics/electronics.

The VCMA as well as SRT process was studied on a typical capacitor heterostructure, Au/[DEME]$^+$[TFSI]$^-$/Pt/(Co/Pt)$_2$/Ta, as illustrated in Figure 1a. With changing the thickness of the cobalt layer around 1 nm, the PMA strength can be effectively controlled.[33,34] Here, the magnetic anisotropy of this film is established near the SRT point, where the magnetic moment tends to rotating from the out-of-plane to the in-plane direction with the increasing Co thickness.[33] The growth rate of Co layers was tested via quartz crystal microbalance (QCM) integrated in the sputtering chamber. The cobalt thickness was precisely controlled at 1.2 nm, and the weak PMA state was evidenced by the six-folder angular-dependent ferromagnetic resonance (FMR) field (H_r) anisotropy investigated from the ESR, as shown by the red line in **Figure 2**a, where the H_r difference between the in-plane direction and the out-of-plane was small.[30] The out-of-plane and in-plane magnetic anisotropy energy difference is negative, and the absolute value is very little. Here, the in-plane antiparallel Rashba fields at the contiguous interfaces equal to each other, resulting in a zero net in-plane Rashba field. The corresponding VSM result also confirms a weak PMA as illustrated in Figures S1 and S2 (Supporting Information). Therefore, the moment switching barrier energy, $\Delta E = E(m\|z) - E(m\|x)$, is much lower than that of the

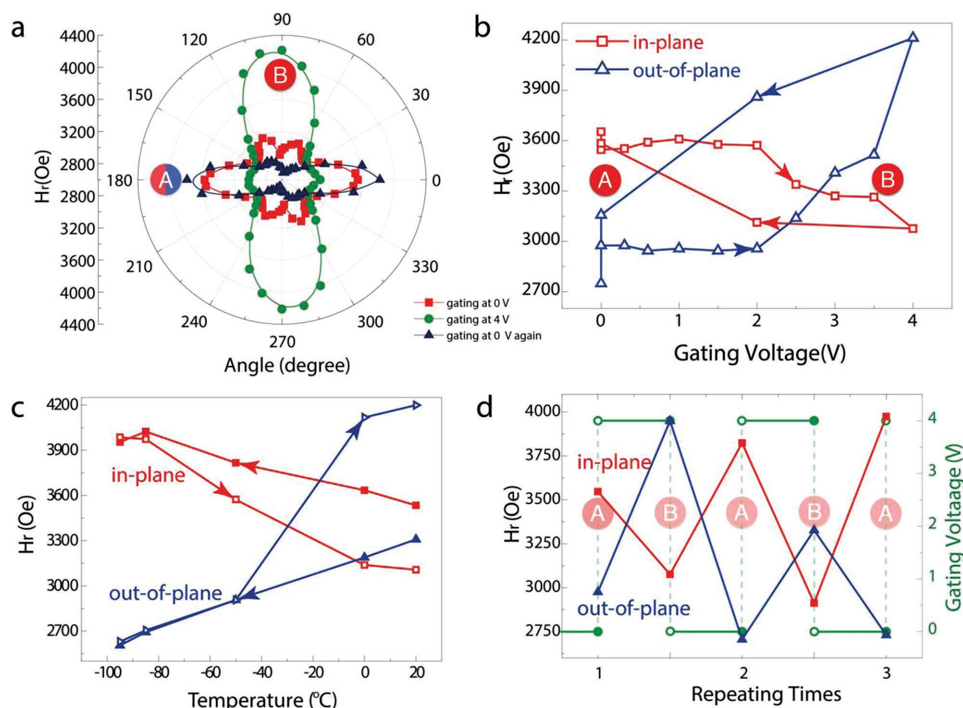

Figure 2. In situ IL gating induced SRT and PMA modulation. a) Angular dependences of the H_r at initial 0 V (red square line), 4 V (green circle line), and final 0 V (blue triangle line), respectively. b) The H_r versus V_g at 0° (in-plane direction, red square line) and 90° (out-of-plane direction, blue triangle line), respectively. c) Temperature dependence of the in-plane (the red square line) and out-of-plane (blue triangle line) H_r during the ionic liquid gating process. The arrows indicate the thermal sequences, and the 4 V gating voltage started applying at −95 °C. d) The reversibility test of the SRT control process. The red square line and the blue triangle line mark the in-plane and out-of-plane H_r switching process, respectively.

© 2018 WILEY-VCH Verlag GmbH & Co. KGaA, Weinheim

strong PMA state, which promises the IL gating modification of SRT and switching of PMA. Here, ΔE is the magnetic anisotropy energy difference, and $E(m\|z)$ and $E(m\|x)$ are magnetic anisotropy energy along z and x directions accordingly.

In situ IL gating modulation of SRT was quantitatively determined via the ESR spectrometer at room temperature as shown in Figure 1b. The resonance fields (H_r) were the null points of the ESR spectrums as plotted in Figure 1c. The out-of-plane FMR intensity of the PMA film was plotted as a function of the external magnetic field (H) and sequential V_g as presented in Figure 1d, the FMR contour diagrams (more details in Figure S3 in the Supporting Information). The intervals were at least 5 min for fully polarizing the IL layer. The black curve unambiguously demonstrates the out-of-plane H_r shift under sequentially applied V_g. Figure 2a gives the spatial FMR information in the in situ gating process via angular-dependent ESR measurements, including the initial state (red square-line; A state), the 4 V gating state (green circle line; B state) and the final 0 V gating state (blue triangle-line; A state), respectively. The initial magnetic moment (easy axis) is normal to the film plane, as shown in Figure 1a, evidenced by $H_{r,in-plane}$ = 3546.75 Oe and $H_{r,out-of-plane}$ = 2959.9 Oe. With increasing V_g, H_r showed no obvious shift until V_g reached 2.5 V, where $H_{r,in-plane}$ starts to decrease, while $H_{r,out-of-plane}$ starts to increase. At $V_g > 2.5$ V, as illustrated in the H_r versus V_g loop of Figure 2b, $H_{r,out-of-plane}$ became larger than $H_{r,in-plane}$, indicating a voltage-induced SRT, where the magnetic easy axis moves toward the in-plane direction (B state). At the 4 V gating state, the easy axis became parallel to the film and the hard axis was switched to the out-of-plane direction, referring to $H_{r,in-plane}$ = 3076.02 Oe, $H_{r,out-of-plane}$ = 4210.97 Oe, and $H_{r,45^\circ}$ = 3057.1 Oe. The IL gating-induced VCMA is 1470 Oe with an out-of-plane ME coefficient of $\alpha_{out-of-plane}$ = 312.76 Oe V^{-1}, which is much greater than previously reported values in ME tuning works.[10–12,27,28,31,32,35] With decreasing V_g, H_r shifted back with a slight hysteresis and then switched back to the initial state, the moment was rotated to the out-of-plane, with $H_{r,in-plane}$ = 3822.94 Oe, and $H_{r,out-of-plane}$ = 2698.36 Oe, corresponding to a record high VCMA of 1572 Oe and an out-of-plane ME coefficient $\alpha_{out-of-plane}$ was 378 Oe V^{-1} during the gating process as demonstrated in Figure 1c. On the contrary, the –4 V gating voltage will enhance the PMA property as shown in Figure S4 in the Supporting Information.

Moreover, the temperature dependence of the IL gating process was confirmed via ESR measurement as shown in Figure 2c and Figure S5 (Supporting Information) in details. With a decreasing temperature, the ungated film performs an enhanced PMA property. From the –95 °C to RT, the test device was gated with 4 V V_g. Above -91 °C, the glass-transition temperature of the $[DEME]^+[TFSI]^-$, the VCMA appeared at -90 °C due to the ionic movement that accumulated at the film surface and the SRT was realized at –30 °C. In addition, the reversible switching of PMA is taken at RT. After several cycles of switching, the difference between $H_{r,in-plane}$ and $H_{r,out-of-plane}$ at 0 V state was enlarged, implying an enhancement of PMA at 0 V state, as depicted in Figure 2d. The Joule heat effect can be excluded due to high cooling performance of the EPR system as mentioned in the Supporting Information.

The IL gating control of SRT switching was also observed in the in situ magnetic hysteresis loop measurements via VSM as shown in Figures S1 and S2 (Supporting Information), which have never been demonstrated before. The Au/$[DEME]^+[TFSI]^-$/Pt/$(Co/Pt)_2$/Ta heterostructure was adapted to a homemade VSM sample holder, which was sealed and separated from the air. Consistent with the initial state in the ESR test, Figure S2 (Supporting Information) demonstrates that the hard axis of the sample is parallel to the film plane, and the out-of-plane magnetic hysteresis loop is easier than that of in-plane. By applying the 4 V V_g, the moment rotates from the out-of-plane (A state) to the in-plane (B state) direction, leading to an in-plane magnetic easy axis. After that, with a 0 V V_g, the hard axis and the magnetic moment can be switched back to the initial PMA state (A state), where the out-of-plane direction is the easy axis. Nevertheless, the VCMA change measured by VSM is smaller than that of ESR method and the reason may be that the continuous vibration interrupted the IL/magnetic interface, leading to a weaker gating effect.

The PMA switching phenomenon was further confirmed via in situ MOKE observation with inert nitrogen protection as shown in **Figure 3**a. The incident spin polarized light was focused on the interface of PMA film/glass substrate, right above the Ta/$(Pt/Co)_2$/Pt/$[DEME]^+[TFSI]^-$/Pt capacitor heterostructure. The Kerr rotation of the incident light also occurred at this interface. The ray of light did not go through the IL layer, which ensured that the possible refractive index change of IL during the polarization cannot affect the MOKE measurement. In this way, we characterized the magnetic property in a more visualized way during the IL gating process as a technical advance. As shown in Figure 3b, at 0 V gating bias (blue-triangle line), the magnetic hysteresis loop from the Kerr signal change under an out-of-plane H-field sweeping indicates that the film was in a PMA state. The domain evolution during the hysteresis loop test was shown in Video S1 in the Supporting Information. With sequentially increased gating bias, the easy axis starts to rotate toward the in-plane direction and displays an obvious loop shape change at 3.2 V (orange-round line). At 3.7 V (red-hexagon), the hysteresis loop demonstrates a typical hard axis property, implying that the IL gating induced a SRT phenomenon. Corresponding to the ESR results, when we withdrew the voltage bias, the easy axis rotated back to the out-of-plane direction. The IL gating effect on PMA film on glass substrate is comparable with the PMA film on silicon substrate, evidenced by in situ EPR measurement as depicted in Figure S7 in the Supporting Information.

Furthermore, the in situ magnetic domain switching observation at fixed H-field (9.13–9.22 mT) gave out clear IL gating-driven domain changing pictures with the assistance of the MOKE microscope as illustrated in **Figure 4**. Before the measurement, the magnetization was fully polarized at –40 mT. Then, the H-field was set to 9.22 mT without any domain change, and the figure was set as background, filling with black color, corresponding to a pure PMA state (state A). Any domain switching would show as bright gray during the gating process. Figure 4 implies the increasing V_g manipulated the magnetization impressively, with 20.00% reversal at 2.5 V, 46.66% reversal at 3.2 V, 59.18% reversal at 3.3 V, 68.40% reversal at 3.5 V, and 100% reversal at 3.7 V. This domain switching process is also

© 2018 WILEY-VCH Verlag GmbH & Co. KGaA, Weinheim

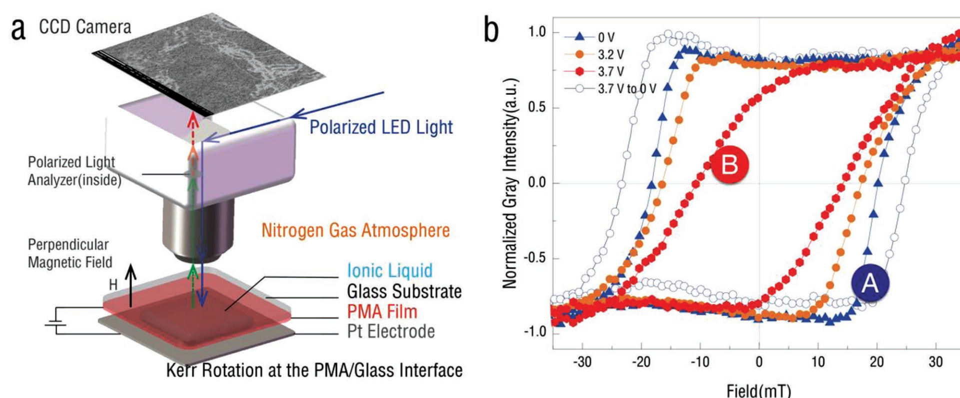

Figure 3. In situ measurement of IL gating induced easy axis rotation via magneto optical Kerr microscope. a) Configuration of in situ MOKE observation. A beam of spin-polarized light is focused at the interface of the glass substrate/PMA film through the objective, above the Ta/$(Pt/Co)_2$/Pt/$[DEME]^+[TFSI]^-$/Pt capacitor heterostructure. The capacitor test devices confined in the inert nitrogen gas atmosphere. The Kerr rotation happens at the interface between the glass substrate and PMA film, and the variation of the spin polarization will be read out through the analyzer and caught by the charge coupled device (CCD) camera. In this way, the gray intensity of the polarized light will be only effected by IL gating induced the interface magnetization change. b) IL gating induced reversible PMA switching characterized by the out-of-plane hysteresis loop revolution from 0 V (blue-triangle line), to 3.2 V (orange-round line), to 3.7 V (red-hexagon line), and then back to 0 V (blue-circle line). The time interval between every two hysteresis is more than 5 min.

reversible and supported by Video S2 as shown in the Supporting Information.

To reveal the physical picture of the voltage control of SRT, we perform a first-principles calculation on a similar system Pt/Co/Pt/Co/Pt/Vac with the interfaces perpendicular to fcc (111) direction, and here "Vac" standing for vacuum as shown in **Figure 5**a. In detail, we fixed the Co lattice translation vector parallel to the interface, same as that of Pt and fully relaxed the distances of each atomic layer inside the system under the condition that the energy converged to $<10^{-6}$ eV and the force converged to 10^{-3} eV Å^{-1}, see more details in the Supporting Information. The calculated coordinates of each atomic layer along z direction can be seen in the Figure 5b, and also the corresponding magnetizations in x and z directions of each atom are plotted with both m$//x$ and $m//z$ cases. We can see that the texture of the magnetization is quite similar to each other except the orientation of the magnetic moment. However, the total energy for these two cases is different, which gives a net energy difference as $\Delta E = E(m\|z) - E(m\|x) \approx -0.015$ meV per atom, which stands for a typical PMA case and the total magnetization is pointing toward out-of-plane direction. After applying an external electric field (0.01 V Å^{-1}) along z direction, the calculation gives $\Delta E = E(m\|z) - E(m\|x) \approx 0.056$ meV per atom, indicating an in-plane magnetization and an E-field induced 90°' magnetization switching. The changing of the magnetization from PMA to in-plane shows a similar result as that from experiments.

Physically, the external electric field will slightly change the distribution of the charge density, which ends up on a changing of the spin–orbit coupling energy ($\Delta E_{so} = E_{so}$ (0.01 V Å^{-1}) $- E_{so}$)

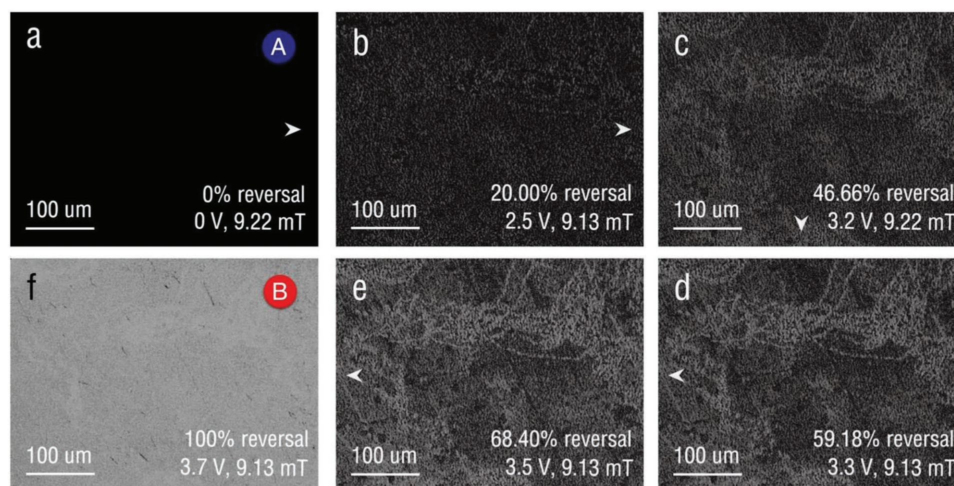

Figure 4. IL gating induced domain switching. The measurement configuration is shown in Figure 3a. The perpendicular external field was set, fluctuated between 9.13 and 9.22 mT due to the small fluctuation of the voltage source. With sequentially increased gating voltage, from: a) 0 V, to b) 2.5 V, to c) 3.2 V, to d) 3.3 V, to e) 3.5 V, to f) 3.7 V, the domain switching was observed and the magnetization reversal percentage was calculated according to the gray intensity of the whole picture. The light gray arrows indicate the sequence of the observation.

© 2018 WILEY-VCH Verlag GmbH & Co. KGaA, Weinheim

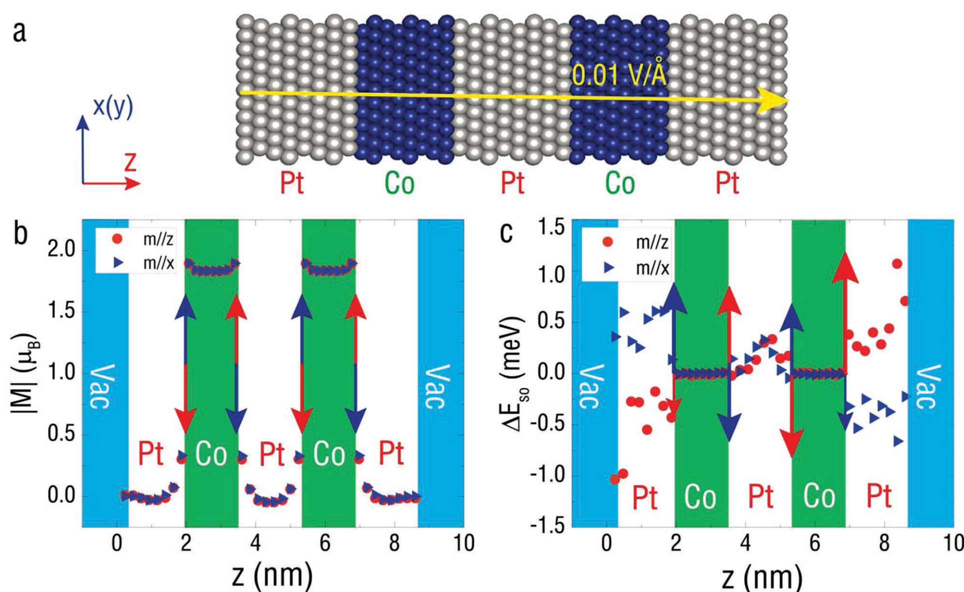

Figure 5. First-principles calculation of the Pt/Co/Pt/Co/Pt/Vac system. a) Schmetic representation of the first-principles calculation of the Pt/Co/Pt/Co/Pt/Vac model. b) The magnetization of each atom in the whole system after fully relaxation on z direction for both $m//z$ (perpendicular to the plane) and $m//x$ (parallel to the plane), the red and blue arrows stand for the Rashba magnetic fields induced by the $m//z$ and $m//x$, respectively. c) The changing of the spin–orbit coupling energy after applying a external electric field (0.01 V Å^{-1}), the changed red and blue arrows stand for the Rashba magnetic fields induced by the in-palne ($m//x$) and out-of-plane ($m//z$) spin–orbital coupling energy change. The arrows were not scaled according to the Rashba field vectors.

across the film as plotted in Figure 5c for both $m//x$ and $m//z$. For an interface between normal metal and ferromagnetic metal, there will be a corresponding in-plane Rashba magnetic field, as shown in the Figure 5b,c with blue and red arrows for both $m//x$ and $m//z$. However, without applying external electric field, the Rashba magnetic field on these four interfaces will vanish due to the symmetric structure,[36] and the PMA dominates in this case, due to the lower energy, as shown in Figure 5b. After applying the external electric field, the spin–orbit coupling strength decrease on the left Pt, while it increases on the right Pt for $m//z$, as represented in Figure 5c. Under an external E-field, there will be a corresponding in-plane Rashba magnetic fields for both $m//x$ and $m//z$. Due to the asymmetric spin–orbit coupling strength, there exist a net in-plane Rashba magnetic field, which forces the magnetization to the in-plane direction.[37] With sufficient E-bias, the changing of the spin–orbit coupling energy overwhelms the PMA energy and leads to a SRT in all probability, which had been observed from our both experiments and confirmed by theoretical calculations.

The electrical property of the IL during the gating process was calibrated with the B2901A Precision Source/Measure Unit within the V_g range (0–4 V), with film surface and Au wire as two electrodes, as shown in **Figure 6**a (see more details in the Experimental Section). It should be noted that the sweeping rate of the voltage was 2 mV s^{-1} in order to reduce the current caused by the ion migration, which was demonstrated by I versus V_g curves. With increasing V_g, the current shows a linear growth, until the $V_g = 2.7$ V; then the current shoots up, corresponding to the electrochemical reaction of [DEME]$^+$[TFSI]$^-$ itself.[38] The capacitance of the capacitor device was measured with the E4980A test unit. Figure 6b illustrates that the surface accumulated charge (Q) increased with the growth gating bias calculated from the equation $Q = CV_g$, which is consistent with the former report.[16] Q saturates at around 3.5 V and stays stable until providing 4 V bias. For a clear comparison, the IL gating-induced FMR shift and magnetization reversal were depicted in the same figure. The H_r and the domain state almost stayed the same until the gating bias was increase to 2.5 V, indicating that the initial surface charge accumulation cannot break the energy barrier of the SRT. The further increasing gating bias gave rise to an obvious in situ VCMA change. Within the electrochemical window of the capacitor device, the VCMA arise from the surface charge accumulation. Between 2.7 and 3.5 V V_g, both charge doping and the electrochemical reaction affect the spin–orbital coupling resulting in a nonzero net Rashba field at the interfaces, and tend to saturate at 3.5 V, implying the charge doping effect dominated in this range. Upon 3.5 V V_g, the electrochemical reaction give rise to the VCMA, deduced from the same trend the I–V, H_r shift versus V and magnetization reversal versus V curves.

After the in situ ESR measurements, the IL and Au wire were removed from the capacitor device, and the film was washed with ethanol for several times. Then, the elemental states and the surface morphology of the samples before and after IL gating were examined with X-ray photoelectron spectroscopy (XPS) and atomic force microscopy (AFM), respectively, as illustrated in Figure S8 in the Supporting Information. In our previous work on IL gating control of the Au/[DEME]$^+$[TFSI]$^-$/Co capacitor devices, a 4 V V_g induced an interfacial electrochemical reaction and damaged the Co surface.[30] In this work, we add a Pt top layer to prevent the Co/Pt interface from IL chemical reaction induced oxidation. The XPS is a sensitive surface elemental characterization method, which measures the kinetic energy and the numbers of the electrons escaping from the top 0–10 nm layer. The XPS results ensure that the elemental

© 2018 WILEY-VCH Verlag GmbH & Co. KGaA, Weinheim

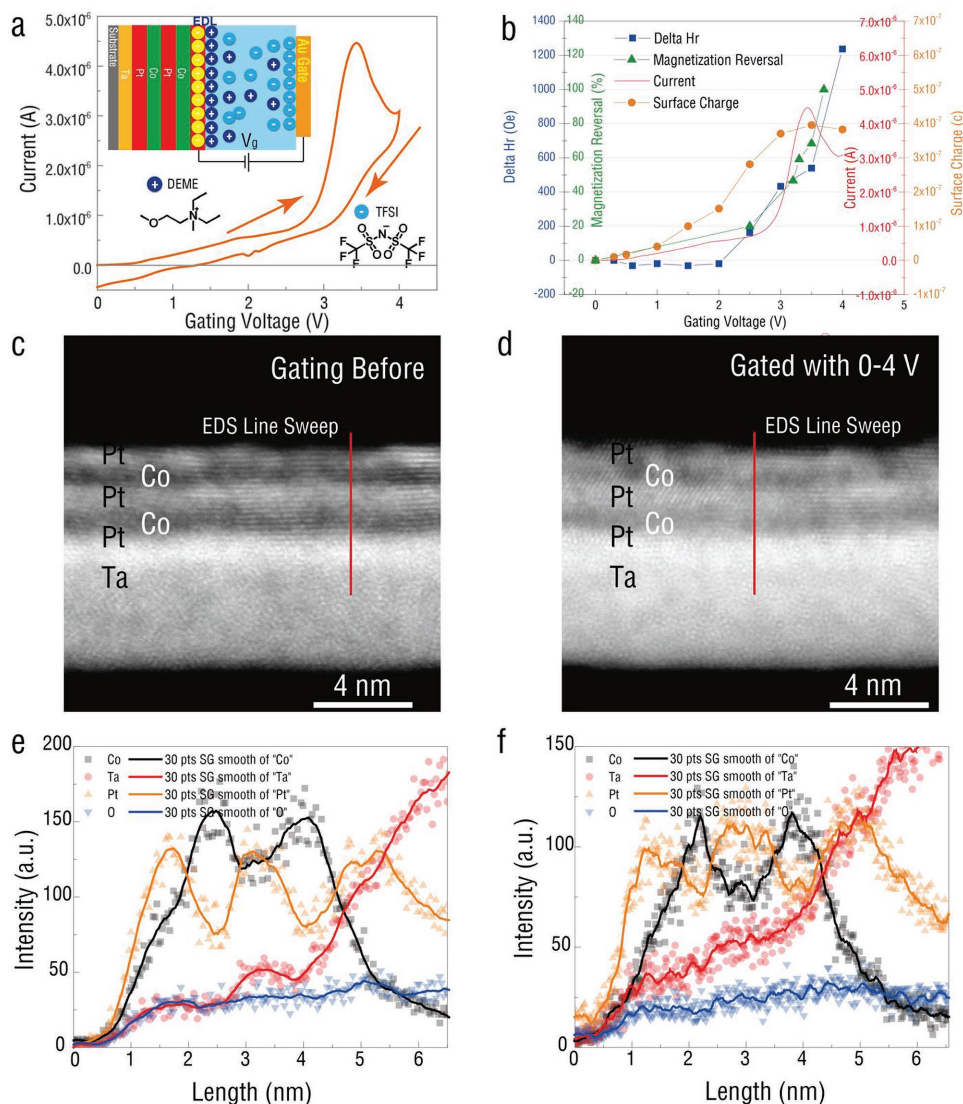

Figure 6. Surface and interface analysis of the PMA films during the IL gating process. a) The current versus gating voltage curve measured by the B2901A Precision Source/Measure Unit. The insets demonstrate the section view of the EDL-assisted IL gating capacitor structure and the molecular formulas of DEME-TFSI. b) The IL gating induced out-of-plane FMR shift (blue-square line), the IL gating induced out-of-plane magnetization reversal at set magnetic field (green-triangle line), the current (red line), and the amount of surface charge at sequentially increasing gating voltages, respectively. c,d) Sectional views of the PMA film before and after gating treatment observed via STEM; e,f) Depth profiles of the elemental composition of the PMA film before and after gating process characterized via the EDS line sweep measurement.

states of Co, O, and Pt in the top layers almost stayed the same; however, a capping layer was induced via IL gating chemical reaction. As revealed by these AFM images in Figure S8 in the Supporting Information, the IL gating process influenced the film surface morphology, leading to a roughness increasing and a slightly damage of the reversibility. As shown in Figure S9 in the Supporting Information, a 3 nm HfO_2 layer was deposited on to the PMA film to enhance the endurance of the capacitor heterostructure, meanwhile the capacitor still showed the PMA switching behavior. Also, the FMR switching reversibility could be greatly enhanced at low temperature as illustrated in Figure S10 in the Supporting Information.

Additionally, we observed the gated and ungated film cross-sections with scanning transmission electron microscope (STEM). Figure 6c,d illustrates the sectional views of PMA heterostructure before and after gating by atomic resolution high angle annular dark field scanning transmission electron microscopy. Figure 6c,d shows that the laminated structures from top to bottom have clear and smooth interfaces, implying that the thickness and roughness could be precisely controlled by the QCM during the sputtering, confirming a well-exhibited PMA structure. Figure 6e,f compares the line sweep energy-dispersive spectrometer (EDS) composition profiles of the interfaces at the gating area before and after the IL gating process. The elemental distributions of cobalt, platinum, and oxygen remained the same. This line sweep EDS measurement gives out depth profile of chemical composition of the PMA films and ensures the stability inside the film.

© 2018 WILEY-VCH Verlag GmbH & Co. KGaA, Weinheim

After analyzing the elemental and structural information, this IL gating process can be explained by the charge doping effect and limited chemical reaction, where the cations move toward the film surface driven by the E-field, resulting in a significant charge accumulation at the film surface.[1,20–23,39,40] Then, the accumulated cations and the inducted negative charges form the EDL, generating an enormous E-field at the interface, which attract the free electrons and then considerably affects the SOC at the interface.[33] The calculation confirmed a voltage tunable SOC strength change and the net Rashba magnetic field at Co/Pt interfaces induced by external E-field led to a PMA toward in-plane magnetization switching. The electrochemical reaction at high voltages accompanied by enhanced charge injection process at the interface. Both the electrostatic charge doping and the electrochemical reaction induced enormous charge; electron absorption weakens the PMA strength of the whole film and switching the SRT correspondingly. Additionally, in this work, with a top Pt layer as protection, the ions of IL can hardly penetrate the surface layer to oxidize Co, even within the IL chemical reaction region, verifying by the surface and interface characterization experimentally. The voltage control of SRT, therefore, was modulated in a reversible and stable way.

In summary, we have realized an IL-gating-controlled SRT modulation, which is characterized by in situ ESR measurements quantitatively and in situ MOKE observation visually. With a small 4 V voltage bias, a large 1572 Oe FMR field shift was achieved and determined, corresponding to a large out-of-plane ME coefficient of 378 Oe V^{-1} and a 3.7 V gating bias reverses the magnetization 100% at 9.2 mT. The magnetic moment could be rotated from the PMA to the in-plane direction reversibly, corresponding to a convincing voltage modulation of SRT process and visible magnetic domain evolution. The first-principles calculation reveals the E-field induced SOC strength change and corresponding SRT due to net Rashba magnetic field at Co/Pt interfaces, resulting in the PMA switching behavior. The XPS and STEM analyses further confirmed the reversibility of the IL gating process, which significantly influenced the SOC effect via interfacial charge accumulation and limited electrochemical reaction. This work opens a door toward tunable IL gating PMA devices such as novel IL memories/transistors.

Experimental Section

Thin-Film Growth: The Pt (0.8 nm)/((Co (1.2 nm)/Pt (0.9 nm))$_2$/Ta (5 nm) multilayer structures were fabricated on surface oxidized silicon substrate via magnetron sputtering at room temperature without further annealing. The growth rate for each material was precisely measured with the QCM and was further confirmed by STEM as shown in Figure 6c. Identical heterostructures were fabricated on glass substrates used for in situ IL gating MOKE measurement.

Device Fabrication: For the in situ ESR measurement, the capacitor devices were shown in Figure 1a. The Pt/(Pt/Co)$_2$/Ta/SiO$_2$ surface and the gold wire (0.1 mm of its diameter and ≈2 mm of its length) were used as two electrodes of the capacitor. $[DEME]^+[TFSI]^-$ (Kanto Chemical Co.) was used as the dielectric layer of the capacitor without further dehydration. The IL was dropped onto the PMA film and confined in a 3 mm × 3 mm × 1 mm chemically inert cell with the gate electrode at the bottom. For the in situ MOKE measurement, the capacitor devices were shown in Figure 3a. PMA film grown on glass substrate and Pt (10 nm)/Ta/Si film were used as two electrodes in the Ta/(Pt/Co)$_2$/Pt/$[DEME]^+[TFSI]^-$/Pt capacitor heterostructure, respectively.

Magnetic Measurements: The in situ VCMA change was quantitatively determined via ESR system (JESFA200, JEOL RESONANCE Inc.). The devices for the in situ ESR measurements were protected in the dry nitrogen gas flow.

The in situ IL gating-induced Kerr signal hysteresis loops revolution and corresponding magnetic domain switching of the Ta/(Pt/Co)$_2$/Pt/$[DEME]^+[TFSI]^-$/Pt capacitor heterostructure were observed via MOKE Microscope (Evico Magnetic Co.). The capacitor structure was protected in dry nitrogen gas flow.

The in situ magnetic hysteresis loops were measured via a Lakeshore 7404 VSM system with a homemade holder. Before the in situ VSM measurement, the capacitor devices were sealed and separated from the air. The voltage was supplied with a B2901A Precision Source/Measure Unit.

Electrical Measurement: The I versus V_g curves were obtained by the B2901A Precision Source/Measure Unit with a 2 mV s^{-1} sweep rate. In this case, the anode was the film surface and the cathode was the Au wire.

The surface charge (Q) versus V_g was measured by E4980A Precision Source/Measure Unit, the capacitor test frequency varied from 21.1 Hz to 2 MHz under different gating voltages. And the value of capacitor was at 21.1 Hz to simulate the condition in the DC IL gating process.

The above two measurements were carried out in a cavity full of dry nitrogen gas, and the devices were same as that used in the ESR measurement.

Surface and Interface Measurement: The analysis of the film surface elemental states was accomplished via a Kratos XPS with 150 W Al anode and a 100 meV step. The morphology of the film surfaces was characterized via a Bruker AFM (Dimension Icon). The film surfaces were cleaned with ethanol before surface characterization. The microstructure of the film was characterized by the scanning transmission electron microscopy (JEOL ARM 200F), equipped with probe spherical aberration corrector. Before the measurement, the ungated and gated samples for the cross-sectional measurement were washed and dried in the air. Then, they were cut and glued before grinding to 15–20 µm. Finally, the thinning step was ended with an ion-milling step (Gatan PIPS 691 precision ion polishing system).

Supporting Information

Supporting Information is available from the Wiley Online Library or from the author.

Acknowledgements

S.Z. and L.W. contributed equally to this work. The work was supported by the Natural Science Foundation of China (Grant Nos. 51472199, 11534015, and 51602244), the National 111 Project of China (B14040), the 973 Program (Grant No. 2015CB057402), and the Fundamental Research Funds for the Central Universities. The authors acknowledge the support from the International Joint Laboratory for Micro/Nano Manufacturing and Measurement Technologies. Z.Z. and M.L. were supported by the China Recruitment Program of Global Youth Experts. Z.-G.Y. primary affiliation is Simon Frasen University (SFU) and the work at SFU was supported by the Natural Science and Engineering Research Council of Canada (NSERC, Grant No. 203773). W.C. gratefully acknowledges financial support from the US Department of Energy, Office of Science, Materials Sciences and Engineering Division.

Conflict of Interest

The authors declare no conflict of interest.

© 2018 WILEY-VCH Verlag GmbH & Co. KGaA, Weinheim

Keywords

ferromagnetic resonance, ionic liquid gating, perpendicular magnetic anisotropy, spin-reorientation transition, voltage control of magnetism

Received: March 13, 2018
Revised: April 12, 2018
Published online: May 29, 2018

[1] U. Bauer, M. Przybylski, J. Kirschner, G. S. D. Beach, *Nano Lett.* **2012**, *12*, 1437.
[2] D. Chiba, S. Fukami, K. Shimamura, N. Ishiwata, K. Kobayashi, T. Ono, *Nat. Mater.* **2011**, *10*, 853.
[3] J.-M. Hu, L.-Q. Chen, C.-W. Nan, *Adv. Mater.* **2016**, *28*, 15.
[4] T. Maruyama, Y. Shiota, T. Nozaki, K. Ohta, N. Toda, M. Mizuguchi, A. A. Tulapurkar, T. Shinjo, M. Shiraishi, S. Mizukami, Y. Ando, Y. Suzuki, *Nat. Nanotechol.* **2009**, *4*, 158.
[5] H. Ohno, D. Chiba, F. Matsukura, T. Omiya, E. Abe, T. Dietl, Y. Ohno, K. Ohtani, *Nature* **2000**, *408*, 944.
[6] M. Weisheit, S. Faehler, A. Marty, Y. Souche, C. Poinsignon, D. Givord, *Science* **2007**, *315*, 349.
[7] Y. Yamada, K. Ueno, T. Fukumura, H. T. Yuan, H. Shimotani, Y. Iwasa, L. Gu, S. Tsukimoto, Y. Ikuhara, M. Kawasaki, *Science* **2011**, *332*, 291.
[8] G. Tian, F. Zhang, J. Yao, H. Fan, P. Li, Z. Li, X. Song, X. Zhang, M. Qin, M. Zeng, *ACS Nano* **2016**, *10*, 1025.
[9] D. Chiba, M. Kawaguchi, S. Fukami, N. Ishiwata, K. Shimamura, K. Kobayashi, T. Ono, *Appl. Phys. Lett.* **2012**, *3*, 888.
[10] M. Liu, B. M. Howe, L. Grazulis, K. Mahalingam, T. Nan, N. X. Sun, G. J. Brown, *Adv. Mater.* **2013**, *25*, 4886.
[11] M. Liu, J. Lou, S. Li, N. X. Sun, *Adv. Funct. Mater.* **2011**, *21*, 2593.
[12] M. Liu, Z. Zhou, T. Nan, B. M. Howe, G. J. Brown, N. X. Sun, *Adv. Mater.* **2013**, *25*, 1435.
[13] J. Lou, M. Liu, D. Reed, Y. Ren, N. X. Sun, *Adv. Mater.* **2009**, *21*, 4711.
[14] B. Cui, C. Song, G. A. Gehring, F. Li, G. Wang, C. Chen, J. Peng, H. Mao, F. Zeng, F. Pan, *Adv. Funct. Mater.* **2015**, *25*, 864.
[15] B. Cui, C. Song, G. Wang, Y. Yan, J. Peng, J. Miao, H. Mao, F. Li, C. Chen, F. Zeng, *Adv. Funct. Mater.* **2014**, *24*, 7233.
[16] H. Du, X. Lin, Z. Xu, D. Chu, *J. Mater. Sci.* **2015**, *50*, 5641.
[17] T. Fujimoto, K. Awaga, *Phys. Chem. Chem. Phys.* **2013**, *15*, 8983.
[18] K. Kita, D. W. Abraham, M. J. Gajek, D. Worledge, *J. Appl. Phys.* **2012**, *112*, 033919.
[19] Y. Liu, G. Agnus, S. Ono, L. Ranno, A. Bernand-Mantel, R. Soucaille, J.-P. Adam, J. Langer, B. Ocker, D. Ravelosona, *J. Appl. Phys.* **2016**, *120*, 023901.
[20] K. Shimamura, D. Chiba, S. Ono, S. Fukami, N. Ishiwata, M. Kawaguchi, K. Kobayashi, T. Ono, *Appl. Phys. Lett.* **2012**, *100*, 122402.
[21] J. Walter, H. L. Wang, B. Luo, C. D. Frisbie, C. Leighton, *ACS Nano* **2016**, *10*, 7799.
[22] Y. J. Zhang, J. T. Ye, Y. Yornogida, T. Takenobu, Y. Iwasa, *Nano Lett.* **2013**, *13*, 3023.
[23] J. T. Ye, Y. J. Zhang, R. Akashi, M. S. Bahramy, R. Arita, Y. Iwasa, *Science* **2012**, *338*, 1193.
[24] Y. Yan, C. Wan, X. Zhou, G. Shi, B. Cui, J. Han, Y. Fan, X. Han, K. L. Wang, F. Pan, *Adv. Electron. Mater.* **2016**, *2*, 1600219.
[25] S. Zhao, Z. Zhou, B. Peng, M. Zhu, M. Feng, Q. Yang, Y. Yan, W. Ren, Z. G. Ye, Y. Liu, *Adv. Mater.* **2017**, *29*, 1606478.
[26] N. P. Lu, P. Zhang, Q. Zhang, R. Qiao, Q. He, H.-B. Li, Y. Wang, J. Guo, D. Zhang, Z. Duan, Z. L. Li, M. Wang, S. Z. Wang, M. Z. Yan, E. Arenholz, S. Y. Zhou, W. L. Yang, L. Gu, C. W. Nan, J. Wu, Y. Tokura, P. Yu, *Nature* **2017**, *546*, 124.
[27] U. Bauer, L. Yao, A. J. Tan, P. Agrawal, S. Emori, H. L. Tuller, S. Van Dijken, G. S. Beach, *Nat. Mater.* **2015**, *14*, 174.
[28] C. Bi, Y. Liu, T. Newhouse-Illige, M. Xu, M. Rosales, J. Freeland, O. Mryasov, S. Zhang, S. te Velthuis, W. Wang, *Phys. Rev. Lett.* **2014**, *113*, 267202.
[29] E. Tamura, J. Van Ek, M. Fröba, J. Wong, *Phys. Rev. Lett.* **1995**, *74*, 4899.
[30] B. Peng, Z. Zhou, T. Nan, G. Dong, M. Feng, Q. Yang, X. Wang, S. Zhao, D. Xian, Z. D. Jiang, *ACS Nano* **2017**, *11*, 4337.
[31] M. Liu, O. Obi, J. Lou, Y. Chen, Z. Cai, S. Stoute, M. Espanol, M. Lew, X. Situ, K. S. Ziemer, V. G. Harris, N. X. Sun, *Adv. Funct. Mater.* **2009**, *19*, 1826.
[32] M. Liu, S. Li, Z. Zhou, S. Beguhn, J. Lou, F. Xu, T. J. Lu, N. X. Sun, *J. Appl. Phys.* **2012**, *112*, 759.
[33] N. Nakajima, T. Koide, T. Shidara, H. Miyauchi, H. Fukutani, A. Fujimori, K. Iio, T. Katayama, M. Yacute, V. Suzuki, *Phys. Rev. Lett.* **1998**, *81*, 5229.
[34] R. C. O'Handley, *Modern Magnetic Materials: Principles and Applications*, John Wiley & Sons, New York **2000**, p. 768.
[35] Z. Zhou, M. Trassin, Y. Gao, Y. Gao, D. Qiu, K. Ashraf, T. Nan, X. Yang, S. Bowden, D. Pierce, *Nat. Commun.* **2015**, *6*, 6082.
[36] G. Bihlmayer, Y. M. Koroteev, P. M. Echenique, E. V. Chulkov, S. Bluegel, *Surf. Sci.* **2006**, *600*, 3888.
[37] H. C. Jang, Y. H. Park, H. C. Koo, H.-j. Kim, J. Chang, H. Kim, *J. Appl. Phys.* **2011**, *109*, 07C313.
[38] T. Sato, G. Masuda, K. Takagi, *Electrochim. Acta* **2004**, *49*, 3603.
[39] C. Song, B. Cui, J. Peng, H. Mao, F. Pan, *arXiv preprint arXiv:1509.01795*, **2015**.
[40] C. Ge, K.-J. Jin, L. Gu, L.-C. Peng, Y.-S. Hu, H.-Z. Guo, H.-F. Shi, J.-K. Li, J.-O. Wang, X.-X. Guo, C. Wang, M. He, H.-B. Lu, G.-Z. Yang, *Adv. Mater. Interfaces* **2015**, *2*, 1500407.

© 2018 WILEY-VCH Verlag GmbH & Co. KGaA, Weinheim